

# Spontaneous Redox Synthesis and Characterization of the Tetrathiafulvalene–Vanadium-Substituted Polyoxometalate Charge-Transfer Material $\text{TTF}_4[\text{SVW}_{11}\text{O}_{40}]$ : Comparison with the Mo Analogue

Qi Li,<sup>†</sup> Jinzhen Lu,<sup>†</sup> John F. Boas,<sup>§</sup> Daouda A. K. Traore,<sup>∇</sup> Matthew C. J. Wilce,<sup>∇</sup> Lisandra L. Martin,<sup>†</sup> Tadaharu Ueda,<sup>\*,‡</sup> and Alan M. Bond<sup>\*,†</sup>

<sup>†</sup>School of Chemistry, Monash University, Clayton, Victoria 3800, Australia

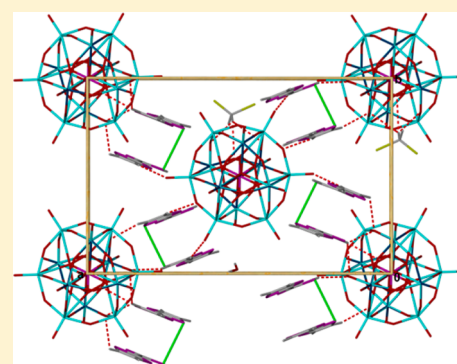
<sup>‡</sup>Department of Applied Science, Faculty of Science, Kochi University, Kochi 780-8520, Japan

<sup>§</sup>School of Physics, Monash University, Clayton, Victoria 3800, Australia

<sup>∇</sup>Department of Biochemistry and Molecular Biology, Monash University, Clayton, Victoria 3800, Australia

## S Supporting Information

**ABSTRACT:** Both conventional solution-phase and direct solid–solid redox reactions between tetrathiafulvalene (TTF) and the vanadium-substituted polyoxometalate  $(n\text{-Bu}_4\text{N})_3[\text{SV}^{\text{V}}\text{W}_{11}\text{O}_{40}]$  give rise to microcrystalline or powdered semiconducting charge transfer solid material. A single-crystal X-ray structure derived from growing crystals from a  $\text{MeCN}-\text{CH}_2\text{Cl}_2$  solution-phase redox reaction gives a stoichiometry of  $\text{TTF}_4[\text{SVW}_{11}\text{O}_{40}]\cdot 2\text{H}_2\text{O}\cdot 2\text{CH}_2\text{Cl}_2$  and reveals that there are two crystallographically different TTF cation moieties based on  $(\text{TTF}_2)^{2+}$  dimers. While the color and morphology of the microcrystalline or powdered  $\text{TTF}_4[\text{SVW}_{11}\text{O}_{40}]$  differ from the single crystals prepared for structural analysis, all materials are spectroscopically (infrared (IR), Raman with respect to the TTF bands, and electron paramagnetic resonance (EPR)) indistinguishable. Raman spectra suggest that the charge transfer is unevenly distributed across the  $(\text{TTF}_2)^{2+}$  dimers, which is postulated to give rise to enhanced mixed-valence features. Structural, spectral, and other properties, such as conductivity, are compared with results available on the recently published molybdenum  $\text{TTF}_4[\text{SVMo}_{11}\text{O}_{40}]\cdot 2\text{H}_2\text{O}\cdot 2\text{CH}_2\text{Cl}_2$  analogue, where the charge distribution is uniform on all TTF cations. In both examples, the position of the V atom is located over several sites. Elemental analysis and voltammetric data also are consistent with the formulations deduced from structural and spectroscopic studies. The conductivity at room temperature is in the semiconducting range, but significantly greater than that for the Mo analogue. EPR spectra at temperatures down to the liquid helium regime confirm the presence of paramagnetic V(IV) and paramagnetic oxidized TTF. The newly isolated  $\text{TTF}-\text{SV}^{\text{IV}}\text{W}_{11}\text{O}_{40}$  material also has magnetic functionality derived from the cationic and anionic components.



## INTRODUCTION

Since the original synthesis of tetrathiafulvalene (TTF) in 1970,<sup>1,2</sup> TTF and its derivatives have become one of the most important electron donor molecules, with thousands of scientific papers being published that describe their synthesis, chemical and physical properties, and applications<sup>3</sup> in molecular electronics,<sup>4</sup> supramolecular chemistry,<sup>5</sup> photoinduced electron transfer,<sup>6</sup> and, more recently, as the redox mediator in dye-sensitized photovoltaics<sup>7</sup> and in Li–O<sub>2</sub> batteries.<sup>8</sup> The first great milestone in the TTF era was marked by the discovery in 1973<sup>9,10</sup> of metallic behavior and other remarkable new properties<sup>11–15</sup> in the charge-transfer complex TTF-TCNQ (where TCNQ = tetracyanoquinodimethane). This discovery stimulated further research work on the synthesis of other TTF-based radical salts that exhibit properties associated with semiconductors, metals, and even superconductors.<sup>11</sup> Recently, metallic conductivity was reported at the interface between the two insulating TTF and TCNQ crystals when they were in

direct mechanical contact;<sup>12,13</sup> an observation that, in turn, generated a new research direction of interfacial phenomena for charge-transfer complexes.

A common goal in the research area of TTF-based charge-transfer complexes is to develop bifunctional solids which exhibit properties that differ from those normally associated with a single material. Materials based on the combination of oxidized TTF and a reduced polyoxometalate (POM) represent one such class that may exhibit bifunctional properties that differ significantly from those found with simple oxidized TTF and reduced POM salts. Polyoxometalate anions are large inorganic clusters. Their rich redox chemistry, along with structural, electronic, magnetic, and photochemical versatility<sup>16–21</sup> make them attractive building blocks for multifunctional hybrid materials. Consequently, hybrid charge-transfer

Received: June 17, 2014

Published: October 1, 2014

complexes containing POM anions and oxidized TTF form an important class of bifunctional materials with properties that have been extensively studied in the past two decades.<sup>16,22–35</sup>

Most commonly, TTF-POM materials have been synthesized by electrocrystallization where TTF was oxidized at an anode in the presence of a POM anion. However, in principle, if the thermodynamics associated with reduction of POM anions can be set up appropriately, TTF-POM materials should become available by spontaneous reaction of TTF and POM, analogously to the reaction between TTF and TCNQ. This was achieved recently in the reaction of TTF and  $(n\text{-Bu}_4\text{N})_3[\text{SVMo}_{11}\text{O}_{40}]$ .<sup>36</sup> In this paper, it is now shown that the vanadium-substituted Keggin-type polyoxometalate  $(n\text{-Bu}_4\text{N})_3[\text{SVW}_{11}\text{O}_{40}]$ , synthesized by vanadium substitution in the parent  $(n\text{-Bu}_4\text{N})_2[\text{SW}_{12}\text{O}_{40}]$  POM provides access to a  $\text{V}^{\text{V/IV}}$  reduction process that has a more positive potential than that for the  $\text{TTF}^{0/+}$  oxidation. This feature allowed the synthesis of charge-transfer TTF-SVW<sub>11</sub>O<sub>40</sub> material in microcrystalline form by rapid spontaneous reaction between solutions of TTF and  $(n\text{-Bu}_4\text{N})_3[\text{SVW}_{11}\text{O}_{40}]$  and powdered form by direct mixing of the TTF and POM solids. Single crystals could be grown from a solution phase redox reaction and structurally characterized by X-ray diffraction (XRD). In terms of the electrical and magnetic bifunctional properties, this newly isolated W-based TTF-POM material like the Mo analogue has interesting properties, from both fundamental and applied perspectives. However, significant differences are found between the newly synthesized and characterized TTF<sub>4</sub>[SVW<sub>11</sub>O<sub>40</sub>] materials and the Mo analogues, with respect to the crystallography, Raman and electron paramagnetic resonance (EPR) spectroscopies, and conductivity. Data from these techniques along with magnetic, electrochemical, and other forms of characterization, are presented in this paper.

## EXPERIMENTAL SECTION

**1. Materials.** Tetrathiafulvalene (TTF, supplied by Aldrich), silver nitrate (Aldrich), ferrocene (Riedel-de Haën), acetonitrile (HPLC grade, Merck) and dichloromethane (CH<sub>2</sub>Cl<sub>2</sub>, HPLC grade, Merck) were used as received from the manufacturer. Tetrabutylammonium hexafluorophosphate  $(n\text{-Bu}_4\text{N})(\text{PF}_6)$  was purchased from Wako Pure Chemical Industries (Japan) and recrystallized from ethanol (95%) and then used as the supporting electrolyte in electrochemical experiments. The vanadium-substituted polyoxometalate  $(n\text{-Bu}_4\text{N})_3[\text{SVW}_{11}\text{O}_{40}]$  was synthesized and purified according to literature procedures with minor modification.<sup>37–39</sup> To a solution containing 8.3 g of Na<sub>2</sub>WO<sub>4</sub>·2H<sub>2</sub>O in 225 mL water was added 10 mL of V(V) stock solution which was prepared by mixing 9.1 g of V<sub>2</sub>O<sub>5</sub>, 4.8 g of NaOH, and 100 mL of water in a Teflon beaker, and 250 mL of MeCN. To this clear solution, 14 mL of concentrated H<sub>2</sub>SO<sub>4</sub> was added dropwise with vigorous stirring. The resultant orange solution was heated in a sealed bottle at 70 °C for 24 h. After cooling to room temperature, 5 g of  $(n\text{-Bu}_4\text{N})\text{Br}$  was added to precipitate an orange salt which is crude  $(n\text{-Bu}_4\text{N})_4[\text{S}(\text{V}_2\text{W}_{10})\text{O}_{40}]$ . This salt was collected by vacuum filtration, washed with water and ethanol, and then air-dried. Then, 2.0 g of crude  $(n\text{-Bu}_4\text{N})_4[\text{S}(\text{V}_2\text{W}_{10})\text{O}_{40}]$  was dissolved in 350 mL of MeCN, followed by the addition of 100 mL of H<sub>2</sub>O. After the addition of 43 mL of concentrated HCl, the resultant orange solution was heated in the sealed bottle at 70 °C for 24 h. When this solution was cooled to room temperature, 5 g of  $(n\text{-Bu}_4\text{N})\text{Br}$  was added to precipitate a bright yellow salt. This salt was isolated by vacuum filtration, washed with a water–ethanol mixture, and air-dried. The salt was further purified by recrystallization at least three times from MeCN.

**2. Voltammetry.** Voltammetric experiments in a conventional three-electrode cell were undertaken at 20 ± 2 °C with a Bioanalytical Systems Model BAS100B electrochemical workstation. Glassy carbon

(3 mm in diameter, Bioanalytical Systems), gold (1 mm in diameter, BAS), and indium tin oxide (ITO)-coated glass (8–12 Ω □<sup>-1</sup> sheet resistance, Delta Technologies, USA) disks were used as the working electrodes. The glassy carbon and gold electrodes were polished with 0.3 μm aqueous alumina slurries, rinsed with distilled water and acetone, and then dried with nitrogen gas. The reference electrode was Ag/Ag<sup>+</sup> [AgNO<sub>3</sub> (10 mM),  $(n\text{-Bu}_4\text{N})(\text{PF}_6)$  (0.1 M) in MeCN, –0.078 V vs Fc/Fc<sup>+</sup>] while Pt wire was used as the counter electrode. Potentials are reported vs the Ag/Ag<sup>+</sup> reference electrode. All solutions were degassed with purified nitrogen gas for 10 min prior to electrochemical experiments.

**3. Solid–Solid-State Synthesis of TTF<sub>4</sub>[SVW<sub>11</sub>O<sub>40</sub>].** An equimolar ratio (e.g., 0.05 mmol) of orange TTF and yellow  $(n\text{-Bu}_4\text{N})_3[\text{SV}^{\text{V}}\text{W}_{11}\text{O}_{40}]$  solids were added into a mortar. Immediately on commencing grinding with a pestle, the orange-yellow color of the mixture changed to dark brown. The mixture of the two solids was ground for 10 min before being rinsed copiously with acetonitrile to remove any unreacted TTF,  $(n\text{-Bu}_4\text{N})_3[\text{SV}^{\text{V}}\text{W}_{11}\text{O}_{40}]$ , or other solid that is soluble in this solvent. The finally isolated powdered solid TTF<sub>4</sub>[SVW<sub>11</sub>O<sub>40</sub>], which is insoluble in acetonitrile, was then collected and vacuum-dried before further analysis.

**4. X-ray Crystallography.** Data were collected at the Australian Synchrotron using the MX1 beamline operating at 15 keV ( $\lambda = 0.7292$  Å). The collection temperature was maintained at 100 K using an open-flow N<sub>2</sub> cryostream. Initial data processing was carried out using XDS software.<sup>40</sup> The structure was solved by direct methods using SHELXS-97.<sup>41</sup> Least-squares refinements against  $F^2$  were carried out using SHELXL-97, using the program X-Seed as a graphical interface.<sup>42</sup> All hydrogen atoms were placed in idealized positions and refined using a riding model.

Crystallographic data for TTF<sub>4</sub>[SVW<sub>11</sub>O<sub>40</sub>]·2H<sub>2</sub>O·2CH<sub>2</sub>Cl<sub>2</sub>: C<sub>26</sub>H<sub>20</sub>Cl<sub>4</sub>O<sub>42</sub>S<sub>17</sub>VW<sub>11</sub>,  $M = 3764.53$ , monoclinic, space group  $C2/c$  (No. 15),  $a = 21.814(4)$  Å,  $b = 13.852(3)$  Å,  $c = 23.160(5)$  Å,  $\beta = 98.16(3)^\circ$ ,  $V = 6927(2)$  Å<sup>3</sup>,  $Z = 4$ ,  $D_c = 3.610$  g/cm<sup>3</sup>,  $F_{000} = 6756$ .  $T = 100(2)$  K,  $2\theta_{\text{max}} = 50.0^\circ$ , 38 581 reflections collected, 6029 unique ( $R_{\text{int}} = 0.0499$ ). Final goodness of fit (GoF) = 1.035,  $R1 = 0.0692$ ,  $wR2 = 0.2383$ ,  $R$  indices based on 6006 reflections with  $I > 2\sigma(I)$  (refinement on  $F^2$ ), 476 parameters, 3 restraints. Lp and absorption corrections were applied;  $\mu = 19.069$  mm<sup>-1</sup>. CCDC File No. 838493 contains the supplementary crystallographic data for this paper and can be obtained free of charge from the Cambridge Crystallographic Data Centre via [www.ccdc.cam.ac.uk/data\\_request/cif](http://www.ccdc.cam.ac.uk/data_request/cif).

**5. Other Instrumentation and Methods.** A Renishaw RM 2000 Raman spectrograph with a 630-nm excitation laser source was used for sample characterization by Raman spectroscopy. FTIR spectra were obtained with a Perkin–Elmer Spectrum instrument, in conjunction with an ATR sampling accessory. <sup>1</sup>H NMR spectra were recorded using a Bruker DPX 300 spectrometer. <sup>1</sup>H resonances were referenced to the residual hydrogen from DMSO-*d*<sub>6</sub> ( $\delta = 2.5$  ppm vs TMS). Scanning electron microscopy (JEOL Model JSM-7001F FEGSEM) was used to obtain images of the solid samples. The sheet resistance of solid samples, from which the conductivity was calculated, was determined using a Jandel RM3-AR four-point probe test meter at 20 ± 2 °C. The thickness was estimated with a Veeco Dektak 150 surface profilometer. Solids for resistance measurements were prepared by drop casting MeCN suspensions of the powdered samples prepared by the solid–solid method onto microscope glass slides and allowing the samples to dry in air. The dried pellets were vacuum pressed at a pressure of 100 MPa by a cold isostatic press before their sheet resistance and thickness were measured. Therefore, the conductivity data reported refers to a microcrystalline sample prepared at very high pressure to give a very dense nonporous solid in which the microcrystals are contacted tightly with each other. The resulting measurements gave highly reproducible conductivity values. Furthermore, compared to the bulk resistance, the contact resistance between microcrystals in such a dense solid pellet is negligible. Hence, the conductivity obtained from the dense pellet is believed to represent the bulk conductivity of the microcrystalline solid material. Importantly, the bulk conductivity at room temperature lies well into the semiconducting range and the comparison with the Mo analogue is

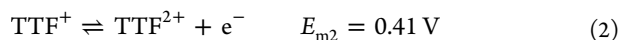
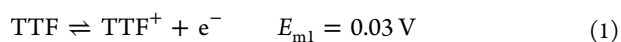
made on the same basis, so the substantial difference (see below) is considered to be significant.

X-band (ca. 9.5 GHz) EPR spectra were recorded with a Bruker Model ESP380E CW/FT spectrometer. Temperatures between 290 K and 110 K were obtained using the standard rectangular TE<sub>102</sub> cavity together with a Bruker Model VT2000 temperature controller and associated nitrogen gas flow insert. Spectra at temperatures between 100 K and 2.6 K were obtained using a Bruker Model ER4118 dielectric resonator inserted in an Oxford Instruments Model CF935 helium cryostat. Temperatures below 100 K were calibrated against a germanium thermometer, using a carbon resistor as a transfer standard. The microwave frequency was measured with an EIP Microwave Model 548A frequency counter and the *g*-values were determined by reference to the F<sup>+</sup> line in CaO (*g* = 2.0001 ± 0.0001).<sup>43</sup> Spectrum simulations were performed using the Bruker XSophe–Sophe–XeprView computer simulation software suite.<sup>44</sup> The experimental spectra were obtained as the first derivative of the absorption, and the spectral intensities were obtained by double integration of the experimental spectrum, using the integration routine in the Bruker WINEPR suite. The quantification of the EPR spectra and correlation with the magnetic susceptibility results through the comparison of integrated intensities is dependent on the assumptions that the field scan range always covers the total width of the resonance and that there is no additional intensity contribution from other species. A further complication is introduced in the present case by the light sensitivity of the TTF<sup>+</sup> radical in the presence of moisture.

Magnetic susceptibility measurements were made with sample masses of ~30 mg using a Quantum Design Model MPMS 5 SQUID magnetometer in dc magnetic fields of 0.01, 0.10, and 1.0 T. Diamagnetic and other corrections were made as described previously using Pascal's constants and other published data as applicable.<sup>36,45</sup>

## RESULTS AND DISCUSSION

**1. Voltammetry of TTF and (n-Bu<sub>4</sub>N)<sub>3</sub>[SV<sup>V</sup>W<sub>11</sub>O<sub>40</sub>] in Acetonitrile.** A voltammetric study was initially conducted on individual solutions of TTF and (n-Bu<sub>4</sub>N)<sub>3</sub>[SV<sup>V</sup>W<sub>11</sub>O<sub>40</sub>] in MeCN (supporting electrolyte, 0.1 M (n-Bu<sub>4</sub>N)(PF<sub>6</sub>)). As described in ref 36 and references cited therein, the voltammogram derived from TTF exhibited two reversible diffusion-controlled, one-electron oxidation processes (eqs 1 and 2) with midpoint potentials of *E*<sub>m1</sub> = 0.03 V and *E*<sub>m2</sub> = 0.41 V (Figure 1).<sup>45,46</sup>



The *E*<sub>m</sub> values (all reported versus Ag/Ag<sup>+</sup>) were calculated from the average of the oxidation *E*<sub>p</sub><sup>ox</sup> and reduction *E*<sub>p</sub><sup>red</sup> peak potentials and equate to the reversible formal potentials *E*<sub>f</sub><sup>0</sup>, assuming that the diffusion coefficients for TTF, TTF<sup>+</sup>, and TTF<sup>2+</sup> are identical, which is a reasonable approximation.<sup>47</sup> In order for the redox reaction that is required to give the TTF<sup>+</sup>-POM charge-transfer material TTF<sub>4</sub>[SV<sup>IV</sup>W<sub>11</sub>O<sub>40</sub>] to be thermodynamically allowable, the reduction of [SV<sup>V</sup>W<sub>11</sub>O<sub>40</sub>]<sup>3-</sup> to [SV<sup>IV</sup>W<sub>11</sub>O<sub>40</sub>]<sup>4-</sup> must occur at a potential that lies between those of the TTF<sup>0/+</sup> and TTF<sup>+2+</sup> oxidation processes. In MeCN (0.1 M (n-Bu<sub>4</sub>N)(PF<sub>6</sub>)) solution, as reported previously,<sup>36</sup> the parent compound (n-Bu<sub>4</sub>N)<sub>3</sub>[SV<sup>V</sup>Mo<sub>11</sub>O<sub>40</sub>] exhibits two well-defined chemically reversible one-electron reduction processes (*E*<sub>m</sub> = 0.148 V and -0.692 V, respectively) under conditions of cyclic voltammetry with the V<sup>V/IV</sup> reduction (*E*<sub>m</sub> 0.148 V) step lying between the TTF<sup>0/+</sup> and TTF<sup>+2+</sup> oxidation. The voltammogram of (n-Bu<sub>4</sub>N)<sub>3</sub>[SV<sup>V</sup>W<sub>11</sub>O<sub>40</sub>] in MeCN (0.1 M (n-Bu<sub>4</sub>N)(PF<sub>6</sub>)) also contains one well-defined V<sup>V/IV</sup> reduction step with *E*<sub>m3</sub> = 0.245 V (eq 3), a value which also meets the

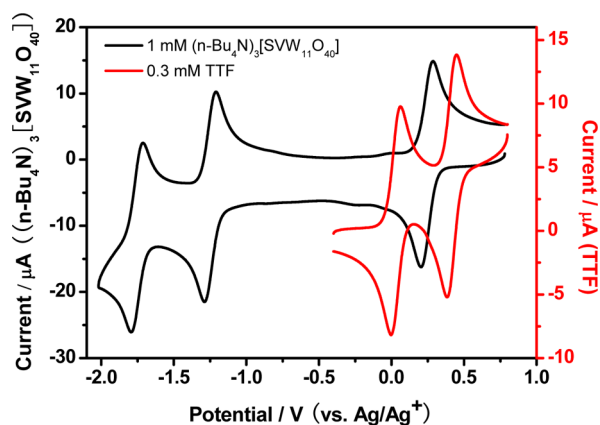
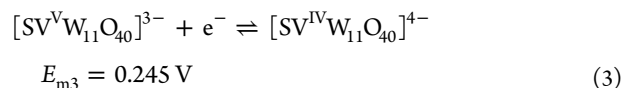
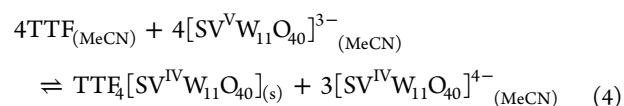


**Figure 1.** Cyclic voltammograms showing a comparison of TTF<sup>0/+</sup> and V<sup>V/IV</sup> processes when TTF (0.3 mM) is oxidized and [SV<sup>V</sup>W<sub>11</sub>O<sub>40</sub>]<sup>3-</sup> (1 mM) is reduced in MeCN (0.10 M (n-Bu<sub>4</sub>N)(PF<sub>6</sub>)). Electrode: glassy carbon (diameter 3 mm). Scan rate = 0.1 V s<sup>-1</sup>.

requirement for a spontaneous reaction with TTF, but with a driving force for the spontaneous reaction significantly greater than applies to the Mo analogue.



This V<sup>V/IV</sup> couple in the W case, which is of direct relevance to this study, is followed by the expected series of W-based reduction processes at more negative potentials (Figure 1). The very small process at -0.041 V and another one of equally small current magnitude at -0.864 V are probably due to the V<sup>V/IV</sup> and W reduction processes of an isomer. The spontaneous reaction of TTF and [SV<sup>V</sup>W<sub>11</sub>O<sub>40</sub>]<sup>3-</sup> which gives oxidized TTF cations and [SV<sup>IV</sup>W<sub>11</sub>O<sub>40</sub>]<sup>4-</sup> is shown as eq 4. The W framework associated POM reduction steps that occur at more negative potentials are not discussed in detail in this study, because they do not contribute to the chemistry of interest.



**2. Solution-Phase Synthesis of Microcrystalline TTF<sub>4</sub>[SV<sup>IV</sup>W<sub>11</sub>O<sub>40</sub>] by Reaction of TTF and (n-Bu<sub>4</sub>N)<sub>3</sub>[SV<sup>V</sup>W<sub>11</sub>O<sub>40</sub>] in MeCN.** Insoluble TTF-SV<sup>V</sup>W<sub>11</sub>O<sub>40</sub> material was prepared by mixing an equimolar (n-Bu<sub>4</sub>N)<sub>3</sub>[SV<sup>V</sup>W<sub>11</sub>O<sub>40</sub>] (1.0 mM) and TTF in MeCN. As also observed<sup>36</sup> for the Mo derivative, the solution rapidly changed to a dark red color and finally a dark brown precipitate was formed. After 1 h, the precipitate was collected by centrifugation. The isolated solid was thoroughly washed with acetonitrile. When a small amount of this solid was placed on a glass slide the SEM image (Figure 2) reveals the presence of many small crystalline microrods (triclinic, orthorhombic, or hexagonal). A few much larger triclinic crystals of size 30 μm × 15 μm × 15 μm also were obtained. Despite the range of morphologies, Raman and IR spectra (see below) derived from all regions of the sample gave the same TTF-based bands.

Square wave voltammetry was used to detect the change in the concentration of the POM upon reaction with TTF. As a reference point, a voltammogram was first obtained for 0.5 mM (n-Bu<sub>4</sub>N)<sub>3</sub>[SV<sup>V</sup>W<sub>11</sub>O<sub>40</sub>] in MeCN (0.1 M (n-Bu<sub>4</sub>N)(PF<sub>6</sub>))



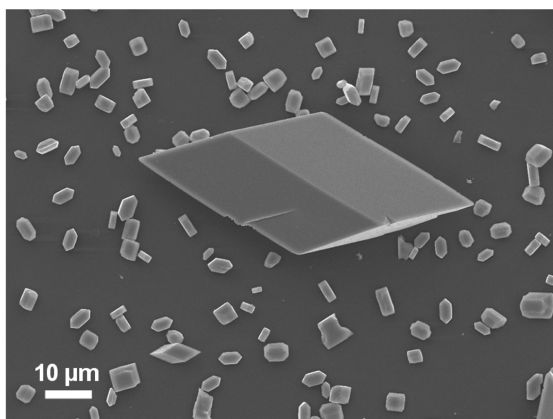


**Figure 2.** An SEM image of TTF-SVW<sub>11</sub>O<sub>40</sub> material formed by mixing (0.10 mM) equimolar TTF and (n-Bu<sub>4</sub>N)<sub>3</sub>[SVW<sub>11</sub>O<sub>40</sub>] solutions in MeCN.

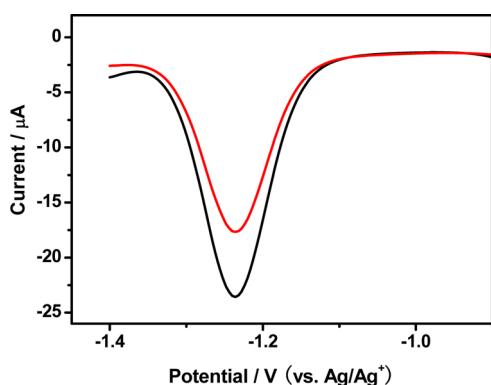


**Figure 3.** Square wave voltammograms in MeCN with 0.1 M (n-Bu<sub>4</sub>N)(PF<sub>6</sub>) in the potential region of the second W-based reduction process for 0.5 mM (n-Bu<sub>4</sub>N)<sub>3</sub>[SVW<sub>11</sub>O<sub>40</sub>] (black) and after reaction of equimolar 0.5 mM (n-Bu<sub>4</sub>N)<sub>3</sub>[SVW<sub>11</sub>O<sub>40</sub>] and TTF (red). Electrode: glassy carbon (diameter = 3 mm). Scan rate = 0.1 V s<sup>-1</sup>.

(Figure 3). The reduction peak at -1.24 V derived from the dissolved POM is due to the initial W-based reduction process, which, according to the voltammetric data in Figure 1, should not contribute to the reaction with TTF. Next, equal volumes of 0.10 mM (n-Bu<sub>4</sub>N)<sub>3</sub>[SVW<sub>11</sub>O<sub>40</sub>] and 1 mM TTF solutions in MeCN (0.10 mM (n-Bu<sub>4</sub>N)(PF<sub>6</sub>)) were mixed to give a solution that initially contained 0.5 mM of each species. The reaction was allowed to continue overnight to ensure that it went to completion. The supernatant solution was then collected and subjected to the square wave voltammetric analysis. Inspection of square wave voltammograms after reaction with 0.5 mM (n-Bu<sub>4</sub>N)<sub>3</sub>[SVW<sub>11</sub>O<sub>40</sub>] (Figure 3) revealed that the peak current for the process at -1.24 V was 25% smaller than before reaction, which is fully consistent with the change predicted by eq 4 if solid TTF<sub>4</sub>[SVW<sub>11</sub>O<sub>40</sub>] has been precipitated.

**3. Reaction between TTF and (n-Bu<sub>4</sub>N)<sub>3</sub>[SVW<sub>11</sub>O<sub>40</sub>] in the Solid State.** The spontaneous reaction between TTF and (n-Bu<sub>4</sub>N)<sub>3</sub>[SVW<sub>11</sub>O<sub>40</sub>] in acetonitrile is predicted on the basis of *E<sub>m</sub>* solution phase values. However, an analogous, but now solventless reaction also occurs spontaneously in the solid state to also give TTF<sub>4</sub>[SVW<sub>11</sub>O<sub>40</sub>] in powdered form, using the procedure described in the Experimental Section. Figure 4 contains photographs of individual samples of TTF and (n-Bu<sub>4</sub>N)<sub>3</sub>[SVW<sub>11</sub>O<sub>40</sub>] and their reacted mixture. A mixture of

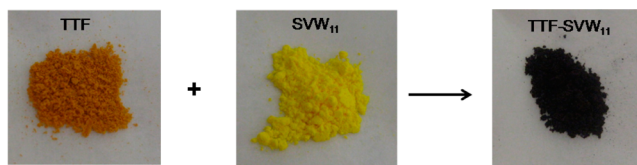
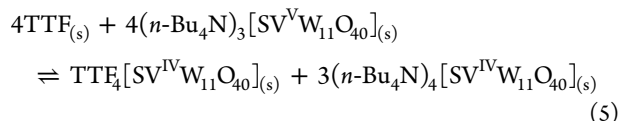


**Figure 4.** Photographs of TTF, (n-Bu<sub>4</sub>N)<sub>3</sub>[SVW<sub>11</sub>O<sub>40</sub>] (SVW<sub>11</sub>), and a mixture of TTF and SVW<sub>11</sub> after grinding them together for 1 min.

TTF and (n-Bu<sub>4</sub>N)<sub>3</sub>[SVW<sub>11</sub>O<sub>40</sub>] (now designated SVW<sub>11</sub>), after grinding, rapidly changes color from yellow-brown (TTF) and yellow (SVW<sub>11</sub>) to dark brown (TTF-SVW<sub>11</sub>), which is indicative of a rapid solid-state reaction between POM and TTF. In the solid state, the reaction given in eq 5 is assumed to have taken place. The reaction product, after washing with copious amounts of acetonitrile to remove soluble (n-Bu<sub>4</sub>N)-POM materials, was dissolved in deuterated DMSO. The <sup>1</sup>H NMR spectra obtained from this solution showed no evidence of the presence of Bu<sub>4</sub>N<sup>+</sup>, which implies that the TTF material obtained in the solid-state reaction is not a mixed cation TTF<sub>x</sub>(n-Bu<sub>4</sub>N)<sub>4-x</sub>[SVW<sub>11</sub>O<sub>40</sub>] (0 < *x* < 3) derivative. This result supports the reaction proposed in eq 5. The TTF bands in the Raman and IR spectra as well as EPR spectral features (see below) are the same, irrespective of whether the complex was prepared via solution-phase or solid-state reactions.



#### 4. X-ray Crystallography of TTF<sub>4</sub>[SVW<sub>11</sub>O<sub>40</sub>]·2H<sub>2</sub>O·2CH<sub>2</sub>Cl<sub>2</sub> and Comparison with the Molybdenum Analogue.

Small square platelike dark blue crystals of TTF<sub>4</sub>[SVW<sub>11</sub>O<sub>40</sub>]·2H<sub>2</sub>O·2CH<sub>2</sub>Cl<sub>2</sub> suitable for X-ray diffraction (XRD) studies were obtained by layering a solution of (n-Bu<sub>4</sub>N)<sub>3</sub>[SVW<sub>11</sub>O<sub>40</sub>] (1.0 mM in MeCN) over a solution of TTF (2.0 mM in MeCN/CH<sub>2</sub>Cl<sub>2</sub>, v:v = 3:1). These crystals had the monoclinic space group C2/c with two crystallographically independent TTF cationic moieties (namely, TTF-A and TTF-B), and a half [SVW<sub>11</sub>O<sub>40</sub>]<sup>4-</sup> anion, one water and one dichloromethane solvates present in the asymmetric unit. The molecular structure of TTF<sub>4</sub>[SVW<sub>11</sub>O<sub>40</sub>]·2H<sub>2</sub>O·2CH<sub>2</sub>Cl<sub>2</sub> is shown in Figure 5a. The crystal is isostructural with its Mo analogue, TTF<sub>4</sub>[SV<sup>IV</sup>Mo<sub>11</sub>O<sub>40</sub>]·2H<sub>2</sub>O·2CH<sub>2</sub>Cl<sub>2</sub><sup>36</sup> (see Table S1 in the Supporting Information). Both structures display a two-dimensional (2D) layered network, consisting of alternating layers of the organic TTF donors and the α-Keggin polyoxometalates (Figure 5b). In general, the reduced [SV<sup>IV</sup>M<sub>11</sub>O<sub>40</sub>]<sup>4-</sup> (M = Mo, W) anion is a structurally typical α-Keggin polyoxometalate anion, which is formed from 12 MO<sub>6</sub> octahedra and one SO<sub>4</sub> tetrahedron. The central S atom is surrounded by four O atoms, with each oxygen site being half-occupied. A feature found in many isolated TTF molecules is the presence of a (TTF<sub>2</sub>)<sup>2+</sup> dimer chain, along the *b*-axis, with the pattern -ABAB- supported by the strong S-S interaction between the TTF-A and the TTF-B, and TTF-B and TTF-A moieties (see Figure 6).

The S-O and M-O bond lengths in the [SV<sup>IV</sup>M<sub>11</sub>O<sub>40</sub>]<sup>4-</sup> anions (M = W or Mo) exhibit little or no difference when experimental uncertainty is taken into account. Thus, the S-O distances lie in the range of 1.394(3)–1.563(3) Å for [SV<sup>IV</sup>W<sub>11</sub>O<sub>40</sub>]<sup>4-</sup> and 1.404(10)–1.567(8) Å for the Mo analogue. In the case of M-O, the distances are 1.658(14)

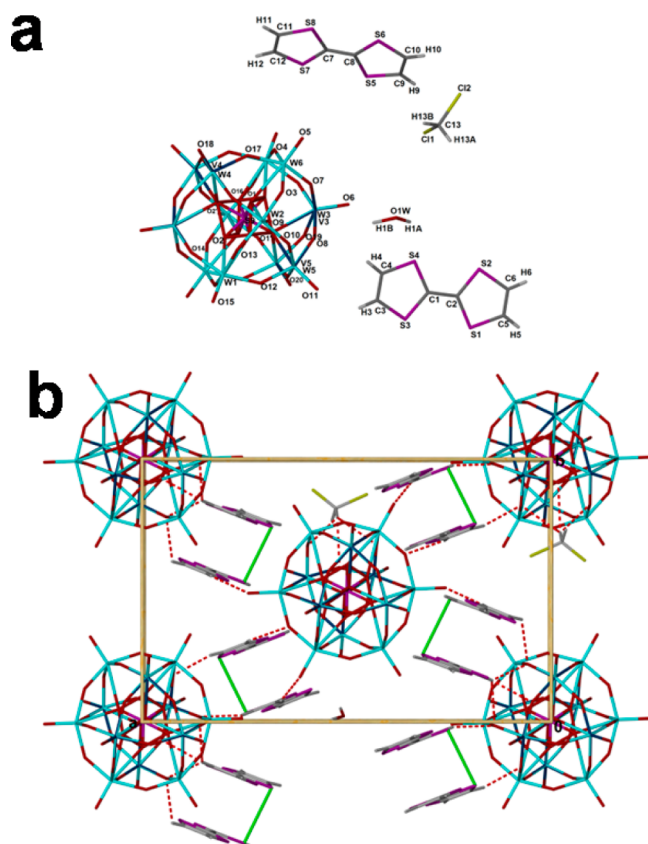


**Figure 5.** X-ray single-crystal structure showing (a) the asymmetric unit of  $\text{TTF}_4[\text{SVW}_{11}\text{O}_{40}] \cdot 2\text{H}_2\text{O} \cdot 2\text{CH}_2\text{Cl}_2$  and (b) the crystal structure viewed along the  $c$ -axis. Red dotted line represents H-bond interactions (Table S2 in the Supporting Information) between the oxygen atoms of POMs and the CH groups in TTF.

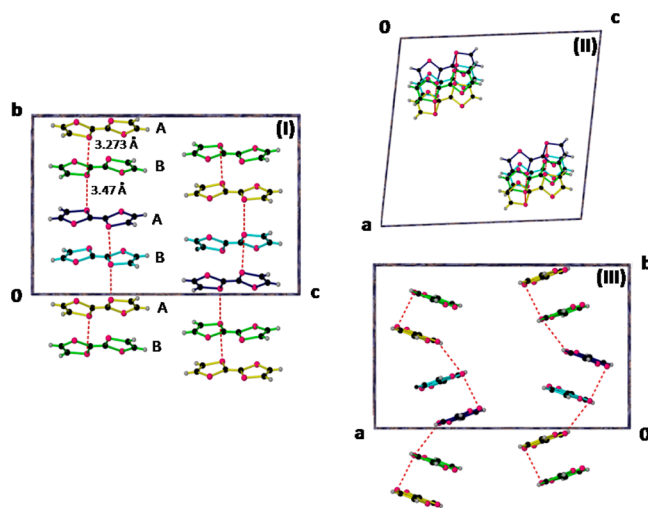


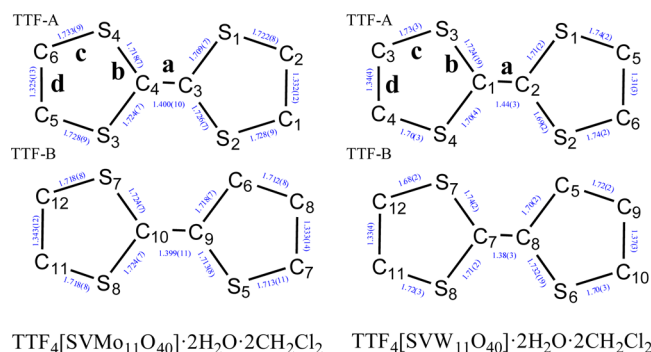
**Figure 6.** TTF chains of dimers in the  $\text{TTF}_4[\text{SVW}_{11}\text{O}_{40}] \cdot 2\text{H}_2\text{O} \cdot 2\text{CH}_2\text{Cl}_2$  crystal structure viewed along (I) the  $a$ -axis, (II) the  $b$ -axis, and (III) the  $c$ -axis.

–1.679(2) Å for  $\text{W}-\text{O}_t$  (terminal), 1.867(2)–1.922(17) Å for  $\text{W}-\text{O}_b$  (bridge), and 2.459(3)–2.528(3) Å for  $\text{W}-\text{O}_c$  (central), compared with 1.648(6)–1.664(6) Å for  $\text{Mo}-\text{O}_t$  (terminal), 1.865(7)–1.947(6) Å for  $\text{Mo}-\text{O}_b$  (bridge), and 2.461(9)–2.513(9) for  $\text{Mo}-\text{O}_c$  (central). Details of the bond

angles for both structures are contained in crystallographic files provided in the Supporting Information.

Although substantial similarities exist between the W and Mo structures, two important differences can be considered: (i) the degree of charge transfer in the TTF cation units and (ii) position disorder of V atoms.

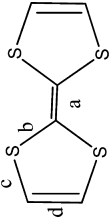
(i) *Analysis of the Degree of Charge Transfer in the TTF Cation Units.* In the W structure, the two crystallographically independent TTF cations in the asymmetric unit are oriented at an angle of  $43.4^\circ$  (see Figures 6) relative to an angle of  $1.44^\circ$  in the Mo analogue.<sup>36</sup> On this basis, it is plausible that the charge transfer degree ( $\rho$ ) differs (Table S3 in the Supporting Information) from that found with the Mo analogue (+1.0 in each case). Unfortunately, the estimated standard deviations (esds) in bond lengths are much greater in the case of the W-POM material, which restricts the reliability of estimates of  $\rho$  in each TTF unit in the W-POM case. Structures of TTF salts often produce large esds in bond lengths<sup>48–54</sup> as also applies to other POMs containing the heavy metal W atom.<sup>55–57</sup> However, where an accurate calculation can be made, consistent trends in the length of the  $\text{C}=\text{C}$  central bond “a” and the  $\text{C}-\text{S}$  bond length “b” of the TTF moieties have been found to be a function of  $\rho$ . As illustrated in Figure 7, generally, the central  $\text{C}=\text{C}$  bond elongates and the average  $\text{C}-\text{S}$  bond shortens in the W derivative.



$\text{TTF}_4[\text{SVMo}_{11}\text{O}_{40}] \cdot 2\text{H}_2\text{O} \cdot 2\text{CH}_2\text{Cl}_2$      $\text{TTF}_4[\text{SVW}_{11}\text{O}_{40}] \cdot 2\text{H}_2\text{O} \cdot 2\text{CH}_2\text{Cl}_2$

**Figure 7.** Bond distances in the TTF cations for  $\text{TTF}_4[\text{SVW}_{11}\text{O}_{40}]$  and its Mo analogue.

Data in Table 1 provide a comparison of the average bond lengths of TTF units in the new  $\text{TTF}_4[\text{SVW}_{11}\text{O}_{40}]$  compound and its Mo analogue with those reported in related examples where the value of  $\rho$  is known with greater certainty. Clearly, the central  $\text{C}=\text{C}$  bond length is most sensitive to charge transfer. Although bond lengths determined by the X-ray crystallography for the W-POM derivative are not accurate enough to reliably estimate the extent of charge transfer in each TTF-POM unit, some differences between TTF-A and TTF-B are found in the central  $\text{C}=\text{C}$  bond distances and the average  $\text{C}-\text{S}$  bond lengths. That is, the  $\text{C}=\text{C}$  bond lengths lie in the range of 1.47–1.41 Å for TTF-A and 1.41–1.35 Å for TTF-B. This feature may imply that the extent of charge transfer in the TTF moieties in the  $\text{TTF}_4[\text{SVW}_{11}\text{O}_{40}]$  is asymmetric, with that in TTF-A being larger than that in TTF-B. The tentative conclusion derived from analysis of the X-ray data that mixed-valence  $(\text{TTF})_2^{2+}$  chains are present is supported by analysis of Raman spectra provided below. By way of contrast, the two crystallographically independent TTF moieties in the asymmetric unit of the Mo analogue lie parallel to each other and the degree of the charge transfer in all cases is close to +1.0, which

Table 1. Degree of Charge Transfer ( $\rho$ ) Calculated from the Mean Bond Lengths in TTF and Its Derivatives


bond [Å]	Bond Lengths (Å)						
	TTF <sup>a</sup>	TTF(ClO <sub>4</sub> ) <sub>4</sub> <sup>b</sup>	TTF(TCNQ) <sup>c</sup>	TTF-A	TTF-B	TTF-A	TTF-B
a	1.349	1.404	1.369	1.400	1.399	1.44	1.38
b	1.757	1.713	1.743	1.719	1.720	1.71	1.72
c	1.726	1.725	1.736	1.728	1.715	1.73	1.71
d	1.314	1.306	1.323	1.329	1.338	1.33	1.35
$\rho$	0	+1	+0.59	+1	+1	$1 < \rho < 2^c$	$0 < \rho < 1^c$

<sup>a</sup>Data taken from ref. S9. <sup>b</sup>Data taken from ref. S2. <sup>c</sup>Data taken from ref. 60. <sup>d</sup>Data taken from ref. 36. <sup>e</sup>Bond lengths used in these calculations were determined from data in the CIF file.

is consistent with the presence of symmetric TTF dimer cations.

(ii) *Position Disorder of Vanadium Atoms.* Although the locations of V and M (M = W, Mo) atoms were observed to be disordered in both TTF-POM structures, they differ crystallographically in the M/V (M = W, Mo) occupancy factors in the mixed atom positions. In the case of the [SVW<sub>11</sub>O<sub>40</sub>]<sup>4-</sup> anion components of the structure, of the six crystallographically unequal W atom locations, three (e.g., W1, W2, and W6) could be assigned as W atoms, whereas the remaining three (W3, W4, and W5) could only be refined as a mixed W/V atom locations with an occupancy factor being 90% for W5 and 80% for W3 and W4, respectively. In this way, the V atom is crystallographically distributed over these three locations with a total 50% atom occupancy in the asymmetric unit cell. In contrast, in the Mo analogue, the vanadium is crystallographically distributed over four Mo atom locations with a total 50% atom occupancy in the asymmetric unit cell and the four Mo atoms are positionally disordered with a population of 90% for Mo1, Mo3, and Mo5 and 80% for Mo2. Disorder also has been observed in the structures of the parent polyoxometalates, (*n*-Bu<sub>4</sub>N)<sub>3</sub>[SVM<sub>11</sub>O<sub>40</sub>] $\cdot$ *x*H<sub>2</sub>O (Mo, *x* = 0.75; W, *x* = 0.5).<sup>58</sup> In the case of (*n*-Bu<sub>4</sub>N)<sub>3</sub>[SVW<sub>11</sub>O<sub>40</sub>] $\cdot$ 0.5H<sub>2</sub>O, nine W atom locations could be assigned as mixed W/V atoms, with an 80% occupancy factor for one W, and a 90% occupancy factor for the remaining eight W atoms. Therefore, in this compound, one V atom is crystallographically disordered over nine W atom sites with the occupancy factors of 20% on one W atom and 10% on the other eight atoms, respectively. In contrast, for the Mo analogue, the V atom is distributed over the four Mo locations with 25% occupancy on each site.

The TTF-SVW<sub>11</sub>O<sub>40</sub> powdered material prepared by the MeCN solution phase reaction was subjected to elemental analysis. On this basis, the solid formed in the reaction mixture in acetonitrile, described above, has a stoichiometry of TTF<sub>4</sub>[SVW<sub>11</sub>O<sub>40</sub>] $\cdot$ 2CH<sub>3</sub>CN. Calculated: C, 9.17; H, 0.60; N, 0.76; S, 14.85. Found: C, 9.35; H, 0.68; N, 0.73; S, 14.9. The presence of MeCN was supported by analysis of the infrared (IR) spectra. Variation in solvates is associated with the different solvents used to prepare the microcrystalline samples and single crystals.

**5. Estimation of the Degree of Charge Transfer in TTF<sub>4</sub>[SVW<sub>11</sub>O<sub>40</sub>] by Raman Spectroscopy.** Given the limitation in the analyses of X-ray data for determining the degree of charge distribution in the TTF moieties, the Raman spectrum of TTF<sub>4</sub>[SVW<sub>11</sub>O<sub>40</sub>] was examined and compared with those obtained for the Mo analogue and TTF (Figure 8), noting that Van Duyne et al.<sup>61</sup> have shown that a well-defined relationship exists between the C=C symmetrical stretching frequency and the redox level in TTF <sup>$\rho$ +</sup>.

Since the *D*<sub>2h</sub> symmetry of TTF does not change significantly upon oxidation, the same assignments of Raman bands (see Figure 8) can be used for TTF and TTF <sup>$\rho$ +</sup>.<sup>61</sup> The vibrational mode *v*<sub>3</sub> (C=C symmetrical stretching) is particularly sensitive to the degree of TTF charge transfer, since it exhibits a large frequency shift upon oxidation.<sup>61–65</sup> In the Raman spectrum of TTF<sub>4</sub>[SVW<sub>11</sub>O<sub>40</sub>] (Figure 8), a *v*<sub>3</sub> band located at 1344 cm<sup>-1</sup> indicates the presence of TTF <sup>$\rho$ +</sup> with  $1 < \rho < 2$ .<sup>65</sup> According to the linear relationship proposed by Van Duyne et al.,<sup>61</sup> this frequency location corresponds to a  $\rho$  value of  $1.7 \pm 0.1$ , which is consistent with the tentative assignment made based on analysis of the X-ray data. However, caution must again be exercised as the TTF-POM derivative is much more complex



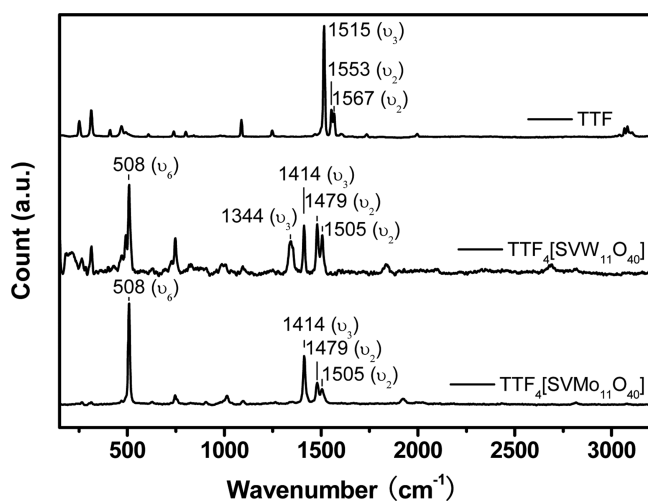


Figure 8. Raman spectra for TTF,  $\text{TTF}_4[\text{SVW}_{11}\text{O}_{40}]$ , and  $\text{TTF}_4[\text{SVMo}_{11}\text{O}_{40}]$  solids.

than the materials considered by Van Duyne et al.<sup>61</sup> Interestingly, the TTF Raman bands for blue  $\text{TTF}_4[\text{SVW}_{11}\text{O}_{40}] \cdot 2\text{H}_2\text{O} \cdot 2\text{CH}_2\text{Cl}_2$  crystals, brown microcrystalline  $\text{TTF}_4[\text{SVW}_{11}\text{O}_{40}] \cdot 2\text{CH}_3\text{CN}$ , or powdered  $\text{TTF}_4[\text{SVW}_{11}\text{O}_{40}]$  are spectroscopically indistinguishable, so the generic form of representation as  $\text{TTF}_4[\text{SVW}_{11}\text{O}_{40}]$  is used in the discussion below.

The Raman spectra of TTF and  $\text{TTF}_4[\text{SVMo}_{11}\text{O}_{40}]$  (significantly simpler than for  $\text{TTF}_4[\text{SVW}_{11}\text{O}_{40}]$ ) and band assignments are also included in Figure 8. The bands at  $1515\text{ cm}^{-1}$  (TTF) and  $1414\text{ cm}^{-1}$  ( $\text{TTF}_4[\text{SVMo}_{11}\text{O}_{40}]$ ) are attributed to the neutral TTF and the  $\text{TTF}^+$  cation ( $\rho = 1$ ), respectively. Significantly, for  $\text{TTF}_4[\text{SVMo}_{11}\text{O}_{40}]$ , there is no band near  $1344\text{ cm}^{-1}$  as in  $\text{TTF}_4[\text{SVW}_{11}\text{O}_{40}]$  and this is the critical outcome of the Raman spectrum, with respect to the hypothesis of a different charge distribution in the W material. The bands at  $1414$  ( $\nu_3$ ),  $1479$  ( $\nu_2$ ),  $1505$  ( $\nu_2$ ), and  $508$  ( $\nu_6$ ), which are characteristic for  $\text{TTF}^+$ , also were observed in the spectrum of  $\text{TTF}_4[\text{SVW}_{11}\text{O}_{40}]$  as in the Mo analogue, but this is not unusual for  $\text{TTF}^{\rho+}$  compounds with  $1 < \rho < 2$ .<sup>65</sup> The fact that the doublet bands ( $1479$  and  $1505\text{ \AA}$ ) were more intense (relative to the intensity of the band at  $1414\text{ \AA}$ ) than those in the Raman spectrum of  $\text{TTF}_4[\text{SVMo}_{11}\text{O}_{40}]$  suggests the possible presence of another unresolved overlapping band, which may be related to  $\text{TTF}^{\rho < 1}$ . However, laser-induced decomposition<sup>65</sup> of  $\text{TTF}^{\rho+}$  may also contribute to the spectrum. Furthermore, IR bands in the TTF region for both the W- and Mo-POM derivatives were very similar, suggesting that detailed theoretical calculations are needed to fully quantify the extent of charge transfer. Given the uncertainty of the exact level of charge transfer, the generic term  $\text{TTF}^+$  rather than fractional charges is employed below in comparing other properties of the overall one-electron-oxidized TTF-W- and TTF-Mo-POM materials.

**6. Conductivity of  $\text{TTF-SVW}_{11}\text{O}_{40}$ .** The sheet resistance of a  $\text{TTF-SVW}_{11}\text{O}_{40}$  solid sample prepared by the solution-phase reaction in acetonitrile was measured by the four-point probe method at room temperature ( $22\text{ }^\circ\text{C}$ ). The conductivity was then calculated to be  $5.5 \times 10^{-5}\text{ S cm}^{-1}$ , which is significantly higher than that of the  $\text{TTF-SVMo}_{11}\text{O}_{40}$  ( $1.6 \times 10^{-6}\text{ S cm}^{-1}$ ), although both values still lie within the semiconducting range.<sup>36</sup> The higher conductivity for the W material, relative to the Mo

analogue, may have its origin from the postulated asymmetric charge transfer distribution.

**7. Magnetic Susceptibility Measurements.** Magnetic susceptibility measurements were undertaken on the polycrystalline  $\text{TTF}_4[\text{SVW}_{11}\text{O}_{40}]$  prepared by the solution-phase reaction method. The temperature dependence of the susceptibility and the magnetic moment are shown in Figure S1 in the Supporting Information. As was the case with  $\text{TTF}_4[\text{SVMo}_{11}\text{O}_{40}]$ ,<sup>36</sup> the temperature dependence of the magnetic moment of the W derivative is more directly informative than the susceptibility. The magnetic moment per formula unit of  $\text{TTF}_4[\text{SVW}_{11}\text{O}_{40}]$  was  $\sim 2.8\ \mu_B$  at  $300\text{ K}$  but decreased with temperature to  $\sim 2.0\ \mu_B$  at  $150\text{ K}$ , less rapidly to a value of  $\sim 1.9\ \mu_B$  at  $50\text{ K}$ , and finally to  $\sim 1.65\ \mu_B$  as the temperature was reduced to  $2.6\text{ K}$ . As was the case for the analogous  $\text{TTF}_4[\text{SVMo}_{11}\text{O}_{40}]$  complex, this temperature dependence indicates the existence of a multicomponent spin system with three regions of magnetic behavior, as discussed below. The magnetic moment was independent of the magnetic field over the temperature range from  $300\text{ K}$  to  $2.6\text{ K}$ , as was also found to be the case for the  $\text{TTF}_4[\text{SVMo}_{11}\text{O}_{40}]$  solid.

**8. EPR Spectroscopy.** Polycrystalline TTF powder exhibited only a very weak EPR resonance of width  $0.96\text{ mT}$  at  $g \approx 2.006$ , associated with a small amount of  $\text{TTF}^+$ . Similarly, polycrystalline powders of  $(n\text{-Bu}_4\text{N})_3[\text{SVW}_{11}\text{O}_{40}]$  exhibited only very weak resonances due to the parallel and perpendicular components of the eight-line hyperfine spectrum, because of the presence of a small number of  $\text{V}^{\text{IV}}$  ions ( $^{51}\text{V}$ ;  $I = 7/2$ ). EPR spectra some 1000 times more intense were obtained at room temperature from the polycrystalline powders obtained by grinding together mixtures of TTF and  $(n\text{-Bu}_4\text{N})_3[\text{SVW}_{11}\text{O}_{40}]$  in the solid state and by crystallization from a mixture of these two components in MeCN solution, although the spectra of the solids obtained by crystallization from MeCN solution were slightly more reproducible than those of solids obtained by the solid-state route.

The EPR spectra recorded at temperatures between  $290\text{ K}$  and  $2.6\text{ K}$  of a polycrystalline powder of  $\text{TTF}_4[\text{SVW}_{11}\text{O}_{40}]$  prepared by the solution-phase reaction and as used for the magnetic susceptibility measurements are shown in Figures 9-I and 9-II. The spectrum at  $290\text{ K}$  exhibited a strong, isotropic resonance with a width of  $\sim 8\text{ mT}$  centered at  $g = 1.987$ . Just as in the case of the  $\text{TTF}_4[\text{SVMo}_{11}\text{O}_{40}]$  described previously,<sup>36</sup> this resonance is ascribed to electrons associated with the oxidized  $\text{TTF}^+$  component. Resonances attributable to the  $\text{V}^{\text{IV}}$  ion were also observed, but were much less intense and could best be observed at high spectrometer gains and at liquid helium temperatures (Figure 9-II). The spectrum at  $2.6\text{ K}$ , shown as Figure 9-IIc, although dominated by the resonance attributed to the oxidized  $\text{TTF}^+$  component, shows a series of less-intense features attributable to  $\text{V}^{\text{IV}}$  ions. These  $\text{V}^{\text{IV}}$  resonances can be approximately matched by a simulated spectrum obtained with the spin Hamiltonian parameters listed in Table 2, as shown in Figure S2 in the Supporting Information. These parameters are similar to those of the one-electron reduced  $[\text{SV}^{\text{IV}}\text{W}_{11}\text{O}_{40}]^{4-}$  solid<sup>58</sup> and are typical for the  $\text{VO}^{2+}$  ion, with the unpaired electron being located in a metal  $3d_{xy}$  orbital. There was no evidence for microwave power saturation broadening at  $2.6\text{ K}$  over the range from  $1\text{ mW}$  down to  $209\text{ nW}$ . No resonances were observed in the vicinity of  $g = 4$  or at lower field, which would have been indicators of direct interactions between electron spins.

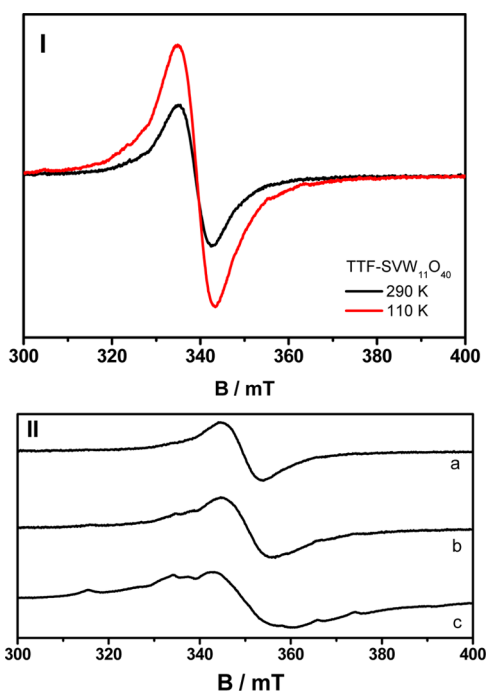


**Figure 9.** (I) EPR spectra of TTF-SVW<sub>11</sub>O<sub>40</sub> at 290 and 110 K. (II) EPR spectra of TTF-SVW<sub>11</sub>O<sub>40</sub> at 80 K (spectrum a), 16 K (spectrum b), and 2.6 K (spectrum c). The lowest field and two highest field parallel resonances due to V<sup>IV</sup> are not shown in the experimental spectra. Microwave frequencies: 9.430 GHz at 290 K, 9.434 GHz at 110 K, 9.715 GHz at 80 K, 9.721 GHz at 15 K, and 9.710 GHz at 2.6 K. Microwave powers: 105  $\mu$ W at 290 and 110 K; 4.18  $\mu$ W at 80, 15, and 2.6 K. Spectrometer gain:  $5.0 \times 10^4$  at 290 and 110 K;  $1.0 \times 10^3$  at 80, 15, and 2.6 K. 100 kHz modulation amplitude (all temperatures): 0.1 mT. Scan range/time (all): 100 mT/83.9 s. Time constants (all): 41 s.

The temperature dependence of the EPR spectrum of TTF<sub>4</sub>[SVW<sub>11</sub>O<sub>40</sub>] is shown in Figure 9 and differs significantly from that of the Mo analogue.<sup>36</sup> As shown in Figure 9, the TTF<sup>+</sup> resonance in TTF<sub>4</sub>[SVW<sub>11</sub>O<sub>40</sub>] is observed from 290 K down to 2.6 K, the lowest temperature reached. Furthermore, as shown in Figures 10a and 10b, respectively, the width of this resonance increases from  $\sim 8.0$  mT at 290 K to  $\sim 14.0$  mT at 2.6 K and the *g*-value decreases from 1.987 to 1.979 over the same temperature range. As shown in Figure 10c, a temperature dependence is also exhibited by the number of EPR detectable spins with  $S = 1/2$  when this is plotted as  $I \times T$ , as a function of  $T$ . The EPR absorption intensity ( $I$ ) is obtained by double integration of the experimental first derivative spectrum, and  $T$  is the absolute temperature. At 290 K, the overall EPR resonance intensity corresponded to  $\sim 1.5$  spins of  $S = 1/2$  per TTF<sub>4</sub>[SVW<sub>11</sub>O<sub>40</sub>] unit and decreased to approximately one-quarter of this value at 2.6 K.

As can be seen from Figure 10, the changes in all three quantities plotted occurred only slowly over the temperature

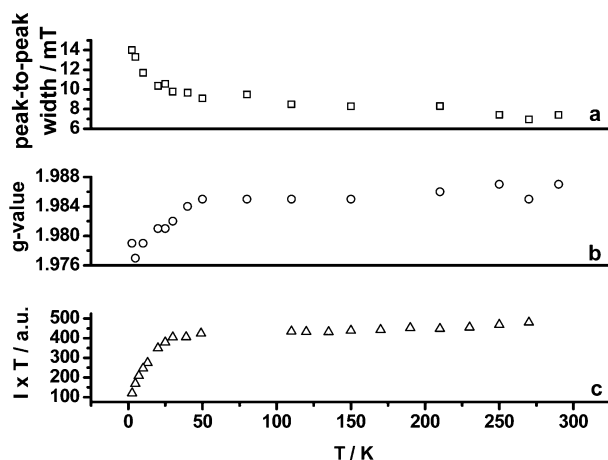


**Figure 10.** (a) Peak-to-peak width, (b) *g*-value, and (c)  $I \times T$  of the EPR spectra of TTF-SVW<sub>11</sub>O<sub>40</sub>, as a function of temperature.

range from 290 K down to  $\sim 50$  K but were more rapid when the temperature was further decreased, and most markedly below  $\sim 30$  K. The changes in *g*-value, line width and  $I \times T$  below  $\sim 50$  K occur over the same temperature range as the decrease in magnetic moment that is shown in Figure S1 in the Supporting Information.

By way of comparison, the TTF<sup>+</sup> resonance in TTF<sub>4</sub>[SVMo<sub>11</sub>O<sub>40</sub>] progressively decreases in intensity as the temperature is reduced from 290 K and is not observed below 110 K. It also does not show a temperature dependence of line width or *g*-value over the temperature range from 290 K to 110 K. Thus, there are significant differences in the EPR spectra, as is also the case with the conductivity and Raman spectra.

**9. Discussion of Magnetism and EPR Data.** Contributions to the magnetic susceptibility and the EPR spectral intensity arise from both unpaired electrons on the V<sup>IV</sup> site occupying part of the polyoxometalate framework and electrons associated with the TTF<sup>+</sup> chains. The latter may be due to both itinerant electrons in the TTF<sup>+</sup> chains and “residual” electrons resulting from localized defects, such as chain ends. Whereas the EPR spectra can distinguish between the unpaired electrons localized on V<sup>IV</sup> sites and those associated with the TTF<sup>+</sup> chains, the magnetic susceptibility measurements cannot distinguish between the contributions from independent spin systems. Thus, the total susceptibility is the sum of the susceptibilities of each of the components. Since the susceptibility at a given temperature is proportional to the square of the magnetic moment, the magnetic moment at a temperature  $T$  of a multicomponent system is proportional to the square root of the sum of the squares of the magnetic moments of each component at that temperature. Therefore, the magnetic moment of two independent spin systems, each with  $S = 1/2$  and  $g = 2$  is  $\sim 2.45 \mu_B$ , not  $2.82 \mu_B$ , as would be the case for a system where two spins with  $S = 1/2$  are coupled to give a  $S = 1$  state. This analysis indicates that the magnetic

**Table 2.** Spin Hamiltonian Parameters of TTF-SVW<sub>11</sub> and SV<sup>IV</sup>W<sub>11</sub> (V<sup>IV</sup> Hyperfine and Quadrupole Interaction Parameters are Given in Units of  $10^{-4} \text{ cm}^{-1}$ )<sup>a</sup>

	$g_x$	$g_y$	$g_z$	$A_x$	$A_y$	$A_z$	$P$
TTF-SVW <sub>11</sub> (this paper)	1.970	1.970	1.907	60.0	60.0	171.0	0.30
SV <sup>IV</sup> W <sub>11</sub> (ref 58)	1.969	1.971	1.908	59.0	62.5	171	0.35

<sup>a</sup>Uncertainties are estimated as follows:  $g$ ,  $\pm 0.002$ ;  $A$ ,  $\pm 2.0 \times 10^{-4} \text{ cm}^{-1}$ ;  $P$ ,  $\pm 0.03 \times 10^{-4} \text{ cm}^{-1}$ .



moment of  $\sim 2.8 \mu_B$  at 300 K is most likely due the presence of more than two unpaired electrons and not simply due to a two-electron state with  $S = 1$ .

In the region above  $\sim 150$  K, the temperature dependence of the magnetic moment indicates the existence of a collection of electron spins coupled by antiferromagnetic interactions with  $|J| \gg 300$  K. The increase in the magnetic moment with temperature above  $\sim 150$  K is attributed to the excitation of electrons from antiferromagnetically coupled states into less tightly bound states where they are able to move along the  $\text{TTF}^+$  chains. Some of these itinerant electrons are responsible for the EPR resonances near  $g = 1.98$ . Although these electrons are primarily associated with the  $\text{TTF}^+$  chains, the shift in  $g$ -value from the  $g \approx 2.010$  for  $\text{TTF}^+$  radical cations<sup>66</sup> is an indicator of delocalization from the  $\text{TTF}^+$  chains onto the polyoxometalate. The shift in  $g$ -value is similar to that occurring in systems where interactions exist between an organic radical and either another organic radical or a paramagnetic cluster.<sup>67,68</sup>

As shown in Figures 9 and 10, the width of the TTF resonance is much larger than the value of  $\sim 1$  mT usually found for isolated  $\text{TTF}^+$  radical cations and cannot be due to the overlap of the electron orbitals with the lowly abundant  $^{183}\text{W}$  isotope ( $I = 1/2$ ; 14.3%). Rather, the line width can be attributed to dipolar interactions between the itinerant electrons, where these interactions are modulated by motional narrowing and exchange interactions. These give rise to an exchange-narrowed resonance line of Lorentzian shape with significant intensity in the wings. Although a quantitative evaluation could not be made because of overlap of the  $\text{TTF}^+$  and  $\text{V}^{\text{IV}}$  components, it appears that the  $\text{TTF}^+$  resonance changes from an essentially Lorentzian shape at  $\sim 290$  K to one with a more Gaussian character at low temperatures. A change in line shape leads to a plausible explanation of the apparent discrepancy between the number of unpaired electrons observed by magnetic susceptibility and EPR spectroscopy. On the basis of this hypothesis, the “missing” EPR intensities may then be interpreted as being due to a greater intensity in the wings of the exchange narrowed resonances as the temperature and, consequently, the number of available unpaired electrons increases. It has been shown that comparisons of integrated intensities are significantly affected when the lineshape function changes from Lorentzian to Gaussian and the intensity residing in the wings of the lines is not properly accommodated in the modelling.<sup>69</sup>

The shift to a larger line width and a lower  $g$ -value as the temperature decreases can also be explained by this model. As the number and mobility of the available electrons decreases, the exchange narrowing effect will become less pronounced and the underlying dipolar interaction between the remaining unpaired electrons more evident. Both effects will lead to an increase in the line width. Furthermore, the decrease in  $g$ -value is attributable to a situation where, although the exchange narrowing averages the  $g$ -values of the TTF and POM components, the decreasing number of electrons in the  $\text{TTF}^+$  chains leads to a greater contribution from localization on the POM framework.

It is noted that the changes in the EPR spectra below 50 K occur in the same temperature region as the decrease in the magnetic moment. Furthermore, Figure 10 implies that the electrons contributing to the  $\text{TTF}^+$  resonance become more delocalized onto the POM framework when the temperature is decreased below  $\sim 50$  K. These observations, when combined

with the decreases in both the magnetic moment and the number of EPR detectable spins, would appear to support the notion of an electron sink, with the interactions between the “leftover” electrons from  $\text{TTF}^+$  engaging in spin pairing with electrons on the  $\text{V}^{\text{IV}}$  site. As was proposed for  $\text{TTF}_4[\text{SVMo}_{11}\text{O}_{40}]$ , the decrease in the magnetic moment and in the number of EPR detectable spins below  $\sim 50$  K may be due to a phase change within the  $\text{TTF}^+$  chains, such as a rearrangement from a dimeric structure to a tetrameric structure. This behavior is similar to that reported for some BEDT-TTF polyoxometalate complexes described by Coronado et al.,<sup>70</sup> although we cannot confirm the existence of a Peierls-like transition in the absence of low-temperature conductivity and structural data.

## CONCLUSION

The new charge-transfer material  $\text{TTF-SVW}_{11}\text{O}_{40}$  has been obtained by the spontaneous reaction of TTF and the polyoxometalate  $(n\text{-Bu}_4\text{N})_3[\text{SVW}_{11}\text{O}_{40}]$  in both solution and solid-state phases. X-ray structural analysis of single crystals of  $\text{TTF}_4[\text{SVW}_{11}\text{O}_{40}] \cdot 2\text{H}_2\text{O} \cdot 2\text{CH}_2\text{Cl}_2$  showed that there are two crystallographically different dimeric  $\text{TTF}^+$  cation units that are both stacked in columns. This asymmetry makes the structure subtly different from that of the Mo analogue. Furthermore, in the case of  $\text{TTF-SVW}_{11}\text{O}_{40}$ , the combination of evidence derived from analysis of the bond lengths obtained by X-ray crystallography and Raman spectra imply that the asymmetric  $(\text{TTF})_2^{2+}$  dimers could plausibly have an asymmetric charge distribution, whereas that in the Mo analogue is symmetric ( $\text{TTF}^+-\text{TTF}^+$ ). The differences in conductivity and EPR behavior could well arise from this difference in charge distribution. The room-temperature conductivities of both the W and Mo microcrystalline samples lie within the semi-conducting range, with that of  $\text{TTF-SVW}_{11}\text{O}_{40}$  being an order of magnitude greater than that of the Mo analogue. Thus, the subtle differences in structure are directly reflected in physicochemical properties and support the notion that the bulk properties of new polyoxometalate (POM) materials can be tuned by framework substitution of different elements in the periodic table.

## ASSOCIATED CONTENT

### Supporting Information

Additional figures and tables. Crystallographic data in CIF format. This material is available free of charge via the Internet at <http://pubs.acs.org>.

## AUTHOR INFORMATION

### Corresponding Authors

\*E-mail: [chuji@kochi-u.ac.jp](mailto:chuji@kochi-u.ac.jp) (T. Ueda).

\*E-mail: [alan.bond@monash.edu](mailto:alan.bond@monash.edu) (A. M. Bond).

### Notes

The authors declare no competing financial interest.

## ACKNOWLEDGMENTS

The authors gratefully acknowledge Prof. K. S. Murray and Dr. B. Moubaraki for magnetic susceptibility measurements, Dr. F. Huang for conductivity measurements and Prof. Stuart Batten and Assoc. Prof. Brendan Abrahams for discussion on the X-ray crystallography. Financial support from the Australian Research Council, under the auspices of the Federation Fellowship (A.M.B.) and Discovery Project (L.L.M., A.M.B.) schemes and

a Grant-in-Aid for Scientific Research from the Ministry of Education, Culture, Sports, Science and Technology of Japan (TU), are acknowledged. The Australian Synchrotron is thanked for provision of beam-time (D.A.K.T., M.C.J.W.), and the Monash Centre for Electron Microscopy is thanked for assistance in obtaining the SEM images.

## REFERENCES

- (1) Wudl, F.; Smith, G. M.; Hufnagel, E. J. *J. Chem. Soc. D—Chem. Commun.* **1970**, 1453.
- (2) Wudl, F.; Wobschall, D.; Hufnagel, E. J. *J. Am. Chem. Soc.* **1972**, *94*, 670.
- (3) *TTF Chemistry: Fundamentals and Applications of Tetrathiafulvalene*; Yamada, J., Sugimoto, T., Eds.; Kodansha, Ltd. (Tokyo) and Springer-Verlag (Berlin, Heidelberg, New York), 2004.
- (4) Martin, N. *Chem. Commun.* **2013**, *49*, 7025.
- (5) Canevet, D.; Salle, M.; Zhang, G. X.; Zhang, D. Q.; Zhu, D. B. *Chem. Commun.* **2009**, 2245.
- (6) Martin, N.; Sanchez, L.; Herranz, M. A.; Illescas, B.; Guldi, D. M. *Acc. Chem. Res.* **2007**, *40*, 1015.
- (7) Yu, Z.; Tian, H. N.; Gabrielsson, E.; Boschloo, G.; Gorlov, M.; Sun, L. C.; Kloo, L. *RSC Adv.* **2012**, *2*, 1083.
- (8) Chen, Y. H.; Freunberger, S. A.; Peng, Z. Q.; Fontaine, O.; Bruce, P. G. *Nat. Chem.* **2013**, *5*, 489.
- (9) Coleman, L. B.; Cohen, M. J.; Sandman, D. J.; Yamagishi, F. G.; Garito, A. F.; Heeger, A. J. *Solid State Commun.* **1973**, *12*, 1125.
- (10) Ferraris, J.; Cowan, D. O.; Walatka, V.; Perlstein, J. H. *J. Am. Chem. Soc.* **1973**, *95*, 948.
- (11) Williams, J. M.; Ferraro, J. R.; Thorn, R. J.; Carlson, K. D.; Geiser, U.; Wang, H. H.; Kini, A. M.; Whangbo, M. H. *Organic Superconductors (Including Fullerenes): Synthesis, Structure, Properties, and Theory*; Prentice Hall: Englewood Cliffs, NJ, 1992.
- (12) Alves, H.; Molinari, A. S.; Xie, H. X.; Morpurgo, A. F. *Nat. Mater.* **2008**, *7*, 574.
- (13) Kirtley, J. R.; Mannhart, J. *Nat. Mater.* **2008**, *7*, 520.
- (14) Xiao, J. C.; Yin, Z. Y.; Li, H.; Zhang, Q.; Boey, F.; Zhang, H.; Zhang, Q. C. *J. Am. Chem. Soc.* **2010**, *132*, 6926.
- (15) Hiraoka, M.; Hasegawa, T.; Yamada, T.; Takahashi, Y.; Horiuchi, S.; Tokura, Y. *Adv. Mater.* **2007**, *19*, 3248.
- (16) Coronado, E.; Gimenez-Saiz, C.; Gomez-Garcia, C. J. *Coord. Chem. Rev.* **2005**, *249*, 1776.
- (17) Hill, C. L. *Angew. Chem.—Int. Ed. Engl.* **2004**, *43*, 402.
- (18) Long, D. L.; Burkholder, E.; Cronin, L. *Chem. Soc. Rev.* **2007**, *36*, 105.
- (19) Mizuno, N.; Misono, M. *Chem. Rev.* **1998**, *98*, 199.
- (20) Rhule, J. T.; Hill, C. L.; Judd, D. A. *Chem. Rev.* **1998**, *98*, 327.
- (21) Yamase, T. *Chem. Rev.* **1998**, *98*, 307.
- (22) Davidson, A.; Boubekur, K.; Penicaud, A.; Auban, P.; Lenoir, C.; Batail, P.; Herve, G. *J. Chem. Soc.—Chem. Commun.* **1989**, 1373.
- (23) Attanasio, D.; Bellitto, C.; Bonamico, M.; Fares, V.; Patrizio, S. *Synth. Met.* **1991**, *42*, 2289.
- (24) Bellitto, C.; Bonamico, M.; Staulo, G. *Mol. Cryst. Liq. Cryst.* **1993**, *232*, 155.
- (25) Bellitto, C.; Staulo, G.; Bozio, R.; Pecile, C. *Mol. Cryst. Liq. Cryst. Sci. Technol. Sect. A* **1993**, *234*, 205.
- (26) Triki, S.; Ouahab, L.; Grandjean, D.; Amiel, J.; Garrigou-Lagrange, C.; Delhaes, P.; Fabre, J. M. *Synth. Met.* **1991**, *42*, 2589.
- (27) Triki, S.; Ouahab, L.; Padiou, J.; Grandjean, D. *J. Chem. Soc.—Chem. Comm.* **1989**, 1068.
- (28) Gomez-Garcia, C. J.; Coronado, E.; Triki, S.; Ouahab, L.; Delhaes, P. *Adv. Mater.* **1993**, *5*, 283.
- (29) Galanmascaros, J. R.; Gimenez-Saiz, C.; Triki, S.; Gomez-Garcia, C. J.; Coronado, E.; Ouahab, L. *Angew. Chem., Int. Ed.* **1995**, *34*, 1460.
- (30) Coronado, E.; Gomez-Garcia, C. J. *Comments Inorg. Chem.* **1995**, *17*, 255.
- (31) Gomez-Garcia, C. J.; Gimenez-Saiz, C.; Triki, S.; Coronado, E.; Lemaguere, P.; Ouahab, L.; Ducasse, L.; Sourisseau, C.; Delhaes, P. *Inorg. Chem.* **1995**, *34*, 4139.
- (32) Coronado, E.; Gomez-Garcia, C. J. *Chem. Rev.* **1998**, *98*, 273.
- (33) Coronado, E.; Galan-Mascaros, J. R.; Gimenez-Saiz, C.; Gomez-Garcia, C. J. *Adv. Mater. Opt. Electron.* **1998**, *8*, 61.
- (34) Coronado, E.; Galan-Mascaros, J. R.; Gimenez-Saiz, C.; Gomez-Garcia, C. J.; Triki, S. *J. Am. Chem. Soc.* **1998**, *120*, 4671.
- (35) Coronado, E.; Galan-Mascaros, J. R.; Gimenez-Saiz, C.; Gomez-Garcia, C. J.; Falvello, L. R.; Delhaes, P. *Inorg. Chem.* **1998**, *37*, 2183.
- (36) Li, Q.; Lu, J. Z.; Boas, J. F.; Traore, D. A. K.; Wilce, M. C. J.; Huang, F. Z.; Martin, L. L.; Ueda, T.; Bond, A. M. *Inorg. Chem.* **2012**, *51*, 12929.
- (37) Himeno, S.; Osakai, T.; Saito, A.; Hori, T. *Bull. Chem. Soc. Jpn.* **1992**, *65*, 799.
- (38) Nambu, J. I.; Ueda, T.; Guo, S. X.; Boas, J. F.; Bond, A. M. *Dalton Trans.* **2010**, *39*, 7364.
- (39) Himeno, S.; Takamoto, M.; Hoshiba, M.; Higuchi, A.; Hashimoto, M. *Bull. Chem. Soc. Jpn.* **2004**, *77*, 519.
- (40) Kabsch, W. *J. Appl. Crystallogr.* **1993**, *26*, 795.
- (41) Sheldrick, G. M. *Acta Crystallogr., Sect. A: Found. Crystallogr.* **2008**, *64*, 112.
- (42) Barbour, L. J. *J. Supramol. Chem.* **2001**, *1*, 189.
- (43) Wertz, J. E.; Orton, J. W.; Auzins, P. *Discuss. Faraday Soc.* **1961**, *31*, 140.
- (44) Hanson, G. R.; Gates, K. E.; Noble, C. J.; Griffin, M.; Mitchell, A.; Benson, S. J. *Inorg. Biochem.* **2004**, *98*, 903.
- (45) Li, Q.; Zhao, C.; Bond, A. M.; Boas, J. F.; Wedd, A. G.; Moubaraki, B.; Murray, K. S. *J. Mater. Chem.* **2011**, *21*, 5398.
- (46) Shaw, S. J.; Marken, F.; Bond, A. M. *Electroanalysis* **1996**, *8*, 732.
- (47) Bond, A. M.; Bano, K.; Adeel, S.; Martin, L. L.; Zhang, J. *ChemElectroChem.* **2014**, *1*, 99.
- (48) Kistenmacher, T. J.; Rossi, M.; Chiang, C. C.; Vanduyne, R. P.; Siedle, A. R. *Inorg. Chem.* **1980**, *19*, 3604.
- (49) Williams, R.; Lowema, C.; Samson, S.; Khanna, S. K.; Somoano, R. B. *J. Chem. Phys.* **1980**, *72*, 3781.
- (50) Ouahab, L.; Bencharif, M.; Mhanni, A.; Pelloquin, D.; Halet, J. F.; Pena, O.; Padiou, J.; Grandjean, D.; Garrigou-Lagrange, C.; Amiel, J.; Delhaes, P. *Chem. Mater.* **1992**, *4*, 666.
- (51) Triki, S.; Ouahab, L.; Halet, J. F.; Pena, O.; Padiou, J.; Grandjean, D.; Garrigou-Lagrange, C.; Delhaes, P. *J. Chem. Soc.—Dalton Trans.* **1992**, 1217.
- (52) Yakushi, K.; Nishimura, S.; Sugano, T.; Kuroda, H.; Ikemoto, I. *Acta Crystallogr., Sect. B: Struct. Crystallogr. Cryst. Chem.* **1980**, *36*, 358.
- (53) Kathirgamanathan, P.; Mazid, M. A.; Rosseinsky, D. R. *J. Chem. Soc.—Perkin Trans. 2* **1982**, 593.
- (54) Triki, S.; Ouahab, L.; Grandjean, D. *Acta Crystallogr., Sect. C: Cryst. Struct. Chem.* **1993**, *49*, 132.
- (55) Mariotti, A. W. A.; Xie, J.; Abrahams, B. F.; Bond, A. M.; Wedd, A. G. *Inorg. Chem.* **2007**, *46*, 2530.
- (56) Fay, N.; Bond, A. M.; Baffert, C.; Boas, J. F.; Pilbrow, J. R.; Long, D. L.; Cronin, L. *Inorg. Chem.* **2007**, *46*, 3502.
- (57) Gomez-Garcia, C. J.; Ouahab, L.; Gimenez-Saiz, C.; Triki, S.; Coronado, E.; Delhaes, P. *Angew. Chem., Int. Ed.* **1994**, *33*, 223.
- (58) Ueda, T.; Nambu, J. I.; Lu, J. Z.; Guo, S. X.; Li, Q.; Boas, J. F.; Martin, L. L.; Bond, A. M. *Dalton Trans.* **2014**, *43*, 5462.
- (59) Cooper, W. F.; Kenny, N. C.; Edmonds, J. W.; Nagel, A.; Wudl, F.; Coppens, P. *J. Chem. Soc. D—Chem. Commun.* **1971**, *16*, 889.
- (60) Kistenmacher, T. J.; Phillips, T. E.; Cowan, D. O. *Acta Crystallogr., Sect. B: Struct. Crystallogr. Cryst. Chem.* **1974**, *30*, 763.
- (61) Van Duyne, R. P.; Cape, T. W.; Suchanski, M. R.; Siedle, A. R. *J. Phys. Chem.* **1986**, *90*, 739.
- (62) Bozio, R.; Girlando, A.; Pecile, D. *Chem. Phys. Lett.* **1977**, *52*, 503.
- (63) Bozio, R.; Zanon, I.; Girlando, A.; Pecile, C. *J. Chem. Phys.* **1979**, *71*, 2282.
- (64) Berlinsky, A. J.; Hoyano, Y.; Weiler, L. *Chem. Phys. Lett.* **1977**, *45*, 419.
- (65) Siedle, A. R.; Candela, G. A.; Finnegan, T. F.; Van Duyne, R. P.; Cape, T.; Kokoszka, G. F.; Woyciejes, P. M.; Hashmall, J. A. *Inorg. Chem.* **1981**, *20*, 2635.

(66) Walsh, W. M.; Rupp, L. W.; Wudl, F.; Kaplan, M. L.; Schafer, D. E.; Thomas, G. A.; Gemmer, R. *Solid State Commun.* **1980**, *33*, 413.

(67) Penicaud, A.; Batail, P.; Perrin, C.; Coulon, C.; Parkin, S. S. P.; Torrance, J. B. *J. Chem. Soc. Chem. Commun.* **1987**, 330.

(68) (a) Resonances with  $g$ -values intermediate between those of an organic radical and an isolated paramagnetic ion in a cluster have been observed by, e.g., Penicaud et al.<sup>67</sup> The  $g$ -value of such a system is given by  $g = g_r\alpha + g_m(1 - \alpha)$ , where  $g_r$  and  $g_m$  are the  $g$ -values of the radical and the magnetic ion in the cluster, respectively, and  $\alpha$  is the electron density on the radical. (b) Tomkiewicz, Y.; Taranko, A. R.; Torrance, J. B. *Phys. Rev. Lett.* **1976**, *36*, 751.

(69) Weil, J. A.; Bolton, J. R.; Wertz, J. E. In *Electron Paramagnetic Resonance: Elementary Theory and Practical Applications*; John Wiley and Sons: New York, 1994; p 497.

(70) Coronado, E.; Clemente-Leon, M.; Galan-Mascaros, J. R.; Gimenez-Saiz, C.; Gomez-Garcia, C. J.; Martinez-Ferrero, E. *J. Chem. Soc.—Dalton Trans.* **2000**, 3955.